

HERCULES STREAM AND THE OUTER ELLIPTICAL RING $R_1 R_2$

A. M. Melnik^{1*}, E. N. Podzolkova^{1,2},

Received February 10, 2025; in final form, March 23, 2025

Abstract — We study the formation of the Hercules stream in the model Galactic disk which includes the outer resonance ring $R_1 R_2$ located near the Outer Lindblad Resonance (OLR) of the bar. The Hercules region and the anti-Hercules region introduced for calibration were restricted in space by the solar neighborhood, $r < 0.5$ kpc, and on the (V_R, V_T) plane by ellipses centered at $V_R = 25$ and $V_T = 200$ km s⁻¹ (Hercules), and at $V_R = -25$ and $V_T = 200$ km s⁻¹ (anti-Hercules). The number of stars in the Hercules region reaches a maximum at the time period of 2–3 Gyr from the start of simulation and the number of stars in the anti-Hercules region oscillates with a period of 1.8 ± 0.1 Gyr. The majority of stars in the model disk located in the Hercules and anti-Hercules regions have orbits elongated perpendicular and parallel to the bar, respectively. The median value of the initial distances of stars in the Hercules (anti-Hercules) region is slightly smaller (larger) than the OLR radius, respectively. There are two types of orbits in the Hercules region. Orbits of the first type always lie inside a figure bounded by two ellipses elongated perpendicular to the bar. Orbits of the second type are elongated at the angles of -60 or 60° to the major axis of the bar most of the time. The distribution of stars in the Hercules region along the period of slow oscillations in the angular momentum has two maxima: $P = 0.7$ and 2.6 Gyr corresponding to orbits of the first and second type. In the anti-Hercules region, most orbits are captured by libration relative to the major axis of the bar with a period of 1.9 Gyr. In general, orbits in the Hercules and anti-Hercules regions support the outer rings R_1 and R_2 elongated perpendicular and parallel to the bar, respectively. Stars from the Gaia DR3 catalog located in the Hercules region appear to be, on average, brighter, bluer and more luminous than stars in the anti-Hercules region which is probably caused by selection effects due to different distributions of these stellar samples over the Galactic latitude b .

Key words: *Galaxy: kinematics and dynamics, Galaxy: neighborhood of the Sun, Gaia DR3*

1. INTRODUCTION

The Hercules stream or the Hercules moving group is a group of stars located near the Sun that move with a high radial velocity away from the Galactic center and with a conspicuously smaller velocity than that of the rotation-curve velocity in the azimuthal direction. The Hercules Stream is often identified on the velocity plane (U, V) , where the positive radial velocity U is directed toward the Galactic center, and the positive azimuthal velocity V is in the sense of the Galactic rotation. The position of the Hercules Stream on the (U, V) plane depends on the accepted values of the velocity components of the solar motion to the apex, but it is often identified as a moving group with a center located near the values $(-40, V_c - 40)$ km s⁻¹ on the (U, V) plane, where V_c is the velocity of the rotation curve at the solar distance (Dehnen, 1998). The Hercules Stream is named after the star ζ Herculis which moves with a similar velocity (Eggen, 1958). In general, the definition of the Hercules Stream remains quite vague.

Hereinafter we will use radial and azimuthal velocities, V_R and V_T , calculated relative to the Galactic center and corrected for the solar motion toward the apex,

where a positive velocity V_R is directed away from the Galactic center and a positive velocity V_T is in the sense of the Galactic rotation.

Modelling of stellar motions in barred galaxies has shown that moving groups similar to the Hercules Stream arise near the Outer Lindblad Resonance (OLR) of the bar. The position of the OLR near the solar circle gives a constraint on the value of the angular velocity of the bar rotation, Ω_b , which must be $\Omega_b \approx 1.9 \Omega_0$, where Ω_0 is the angular velocity of the Galactic-disk rotation at the solar distance (Dehnen, 2000; Fux, 2001; Minchev, Nordhaus, and Quillen, 2007; Antoja et al., 2014; Monari et al., 2017; Hunt et al., 2018).

Alternative conceptions are that the Hercules Stream is caused by the presence of spiral arms in the Galaxy (Michtchenko et al., 2018), or by the motion of stars in the banana-shaped orbits near the Corotation Radius (CR) of the bar (Perez-Villegas et al., 2017), or by a collective perturbation caused by the bar and the spiral arms (Chakrabarty and Sideris, 2008; Hattori et al., 2019).

Bensby et al. (2007) found that stars in the Hercules Stream have a large range of ages and metallicities. Modern studies with the use of the LAM-

*e-mail: anna@sai.msu.ru

OST, APOGEE, and GALAH data have shown that the metallicity of the Hercules-Stream stars is, on average, slightly higher than the metallicity of the stars in the surrounding disk (Quillen et al., 2018; Liang et al., 2023).

The use of the Gaia data (Prusti et al., 2016; Brown et al., 2021; Vallenari et al., 2023) has provided an opportunity to divide finer structure within the Hercules stream (Ramos, Antoja, and Figueras, 2018; Lucchini et al., 2023).

We study the formation of the Hercules stream using the model of the Galaxy in which the disk forms an outer resonance ring R_1R_2 located near the OLR of the bar (Schwarz, 1981; Buta and Crocker, 1991; Byrd et al., 1994; Buta, 1995; Buta and Combes, 1996; Rautiainen and Salo, 1999; Rautiainen & Salo, 2000; Melnik and Rautiainen, 2009; Rautiainen and Melnik, 2010; Melnik, 2019). The elliptical ring R_1 lies slightly closer to the Galactic center and is stretched perpendicular to the bar while the elliptical ring R_2 is located slightly farther away from the Galactic center and is elongated parallel to the bar. The backbone of the resonance rings are periodic orbits near which there are a large number of quasi-periodic orbits (Contopoulos and Papayannopoulos, 1980; Contopoulos and Grosbol, 1989).

Weinberg (1994) showed that near the Lindblad resonances of the bar there are orbits that periodically change the direction of their elongation relative to the bar major axis. Besides, the angular momentum and the total energy of stars change with the same period. We found that librations of the direction of orbit elongation cause periodic changes in the morphology of the outer rings and the appearance of humps on the profiles of the V_R -velocity distribution along the distance R (Melnik, Podzolkova, and Dambis, 2023; Melnik and Podzolkova, 2024). Orbits captured by resonances of the bar can also create other kinematical features (Fragkoudi et al., 2019; Chiba, Friske, and Schönrich, 2021; Trick et al., 2021; Drimmel et al., 2023).

2. MODEL

We use a 2D model of the Galaxy with an analytical bar (de Vaucouleurs and Freeman, 1972; Athanassoula et al., 1983; Pfenniger, 1984) which reproduces best the distributions of the radial, V_R , and azimuthal, V_T , velocities along the Galactocentric distance, R , derived from the Gaia EDR3 and Gaia DR3 data (Melnik et al., 2021). The model includes the bar, exponential disk, classical bulge and halo. The masses of the bar, disk and bulge are 1.2×10^{10} , 3.25×10^{10} and $5 \times 10^9 M_\odot$, respectively. The model has a flat rotation curve on the periphery, and the angular velocity of the model-disk rotation at the distance of the Sun

is $\Omega_0 = 30 \text{ km s}^{-1} \text{ kpc}^{-1}$. The bar rotates with the angular velocity of $\Omega_b = 55 \text{ km s}^{-1} \text{ kpc}^{-1}$ which corresponds to the positions of the CR and OLR of the bar at $R_{RC} = 4.04$ and $R_{OLR} = 7.00 \text{ kpc}$. The resonance $-4/1$ of the bar lies at a distance of $R_{-4/1} = 5.52 \text{ kpc}$. The strength of the bar (the maximum ratio of the amplitude of the tangential force to the average radial force at the same radius) is $Q_b = 0.3142$ which allows us to classify it as a moderately strong bar (Block et al., 2001; Buta, Laurikainen, and Salo, 2004; Díaz-García et al., 2016). The bar turns on gradually, gaining its full strength in 4 bar rotation periods, which corresponds to a growth time of $T_g = 0.45 \text{ Gyr}$. The model contains 10^7 particles. The simulation time is 6 Gyr.

The best agreement between the model and observations corresponds to the position angle of the Sun relative to the major axis of the bar of $\theta_\odot = -45^\circ$. Since our model has the order of symmetry $m = 2$, both values of the position angle, $\theta_\odot = -45^\circ$ and 135° , are equivalent (for more details see Melnik et al., 2021).

The time intervals at which the model and observations agree best correspond to the periods $t = 2.5 \pm 0.3$ and $4.5 \pm 0.5 \text{ Gyr}$ from the start of simulation, when the humps on the profiles of the V_R -velocity distribution disappear (Melnik and Podzolkova, 2024). Hereinafter, we will use the time period of $t = 2.5\text{--}2.6 \text{ Gyr}$ to compare the model and observations.

3. OBSERVATIONS

We consider stars from the Gaia DR3 catalog (Prusti et al., 2016; Katz et al., 2018; Brown et al., 2021; Vallenari et al., 2023) located at the distance $r < 0.5 \text{ kpc}$ from the Sun and near the Galactic plane, $|z| < 0.2 \text{ kpc}$, having the parallax to parallax error ratio $\varpi/\varepsilon_\varpi > 5$, the error RUWE < 1.4 and the line-of-sight velocity V_r measured by the Gaia spectrometer. Fig. 1 shows the distribution of the observational sample of stars on the (V_R, V_T) plane. The color shows the ratio of the number of stars in the $2 \times 2 \text{ km s}^{-1}$ areas to the average number of stars in the areas containing at least 10 stars. It is clearly seen that the observational distribution is elongated towards positive values of the velocity V_R and low values of the azimuthal velocity V_T .

It is quite difficult to compare directly the model and observations. First, the observational and model samples have different numbers of objects. Second, the observational sample includes stars of the thick disk and halo, which are absent in the model sample. Third, the observational sample is burdened by selection effects, the main one of which is related to the selection of stars with a known line-of-sight velocity V_r .

The effective limit on the measurement of magnitudes G and astrometry of Gaia is 1 050 000 sources/degree² (Prusti et al., 2016). When the Gaia processing pro-

gram chooses which of two stars to assign a measurement window to, it will always choose the brighter star, so the crowding of stars reduces the completeness of the catalog due to lack of faint objects. The size of the windows for measuring BP/RP photometry and line-of-sight velocities is even larger, so the limits on the number of simultaneously measured objects are lower here and equal to 750 000 and 35 000 sources/degree², respectively. The probability that the Gaia spectrometer will successfully measure the line-of-sight velocity, V_r , of a star depends on its magnitude G_{RVS} , color $G - G_{RP}$ and the density of bright stars in a given region of the sky (Boubert and Everall, 2020; Rybizki et al., 2021; Everall and Boubert, 2022; Castro-Ginard et al., 2023).

To calibrate the number of stars, we use the anti-Hercules region located symmetrically to the Hercules region relative to the line $V_R = 0$. Fig. 1 shows the positions of the Hercules and anti-Hercules regions which are restricted by ellipses with centers at $V_R = 25$ and $V_T = 200 \text{ km s}^{-1}$ (Hercules), and at $V_R = -25$ and $V_T = 200 \text{ km s}^{-1}$ (anti-Hercules) and semi-axes of $\Delta V_R = 15$ and $\Delta V_T = 12 \text{ km s}^{-1}$. In addition, we excluded from consideration stars with a high vertical velocity V_z , $|V_z| > 50 \text{ km s}^{-1}$. The velocity dispersion of Gaia DR3 stars in the vertical direction at the solar distance is $\sigma_z = 15.46 \text{ km s}^{-1}$, therefore the restriction $|V_z| > 50 \text{ km s}^{-1}$ corresponds to $\sim 3\sigma$. This resulted in exclusion of 1.3 and 2.2% stars from the Hercules and anti-Hercules regions, respectively. The final samples of Gaia DR3 stars in the Hercules and anti-Hercules regions include 148 404 and 108 005 objects, respectively (see also Section 4.7).

When calculating the V_R , V_T and V_z velocities relative to the Galactic center (Melnik et al., 2021, Eq. 3, 4 and 5), we use the following data for the solar motion. The components of the solar motion in the direction toward the Galactic center, in the sense of the Galactic rotation and perpendicular to the Galactic plane, as well as the angular velocity of the disk rotation at the solar distance are taken to be $(U_\odot, V_\odot, W_\odot) = (10, 12, 7) \text{ km s}^{-1}$ and $\Omega_0 = 30 \text{ km s}^{-1} \text{ kpc}^{-1}$, respectively, which is consistent with the kinematics of OB associations (Melnik and Dambis, 2020).

The Galactocentric distance of the Sun is adopted to be $R_0 = 7.5 \text{ kpc}$ (Glushkova et al., 1998; Nikiforov, 2004; Eisenhauer et al., 2005; Bica et al., 2006; Nishiyama et al., 2006; Feast et al., 2008; Groenewegen, Udalski, and Bono, 2008; Reid et al., 2009; Dambis et al., 2013; Francis and Anderson, 2014; Boehle et al., 2016; Branham, 2017; Iwanek et al., 2023). In general, the choice of R_0 in the range of 7–9 kpc has practically no effect on our results. With this choice of R_0 , the azimuthal rotation velocity of the disk at the solar distance is $V_T = 225 \text{ km s}^{-1}$.

4. RESULTS

4.1 Distribution of model stars on the (V_R, V_T) plane at different time periods

The Hercules region forms rather slowly in the model disk. Fig. 2 shows the distribution of model stars located at the distance of $r < 0.5 \text{ kpc}$ from the Sun on the (V_R, V_T) plane at the different time periods. We divided the region $-80 < V_R < 80$ and $160 < V_T < 270 \text{ km s}^{-1}$ into $2 \times 2 \text{ km s}^{-1}$ areas, calculated the number of stars n in each area at different times and compared them with the average number of stars, \bar{n} , in areas containing at least one star, $n \geq 1$, in the range $-80 < V_R < 80$ and $160 < V_T < 270 \text{ km s}^{-1}$. As the ratio n/\bar{n} increases, the color of the area changes (see the color palette on the right).

We consider the time periods of $t = 0\text{--}100, 1000\text{--}1100, 1500\text{--}1600$, and $2500\text{--}2600 \text{ Myr}$ from the start of simulation. To increase the number of stars in the model sample, we sum up the number of stars n that fall into the circle $r < 0.5 \text{ kpc}$ at 10 time instants separated from each other by 10 Myr within the time interval of 100 Myr. At each of the moments considered, the circle $r < 0.5 \text{ kpc}$, where r is the heliocentric distance, includes different stars.

The position angle of the Sun relative to the major axis of the bar is adopted to be $\theta_\odot = 135^\circ$. In the reference frame of the bar, stars at the distance of the Sun rotate in the direction opposite that of Galactic rotation with the average velocity of $R_0(\Omega_0 - \Omega_b)$, which is 188 km s^{-1} . Over 10 Myr, they move on average by 1.9 kpc, which is significantly larger than the size of the circle of $r < 0.5$. In general, this estimate is obtained for circular orbits, but real orbits may have loops. However, verification showed that the total sample does not actually include the same stars at different time moments.

Fig. 2 shows that the distribution of stars on the (V_R, V_T) plane changes over time. At the initial moment, the distribution of stars has an elliptical shape with the center at $V_R = 0$ and $V_T = \Omega_0 R_0 - 7 = 218 \text{ km s}^{-1}$. The difference -7 km s^{-1} between the most probable velocity at the initial moment and the velocity of the rotation curve, $\Omega_0 R_0$, is a consequence of the asymmetric drift (for example, Binney and Tremaine, 2008). We can clearly see that the distribution of stars changes with time forming branches located both to the right and to the left from the central condensation. The so-called Hercules stream corresponds to the positive radial velocities of $20\text{--}30 \text{ km s}^{-1}$ and azimuthal velocities of $V_T \approx 200 \text{ km s}^{-1}$, lagging behind the rotation curve velocity ($V_c = 225 \text{ km s}^{-1}$) by $\sim 25 \text{ km s}^{-1}$. For clarity, we define the Hercules stream as the region within an ellipse centered at $V_R = 25$ and $V_T = 200 \text{ km s}^{-1}$ and semi-axes of $\Delta V_R = 15$ and $\Delta V_T = 12 \text{ km s}^{-1}$.

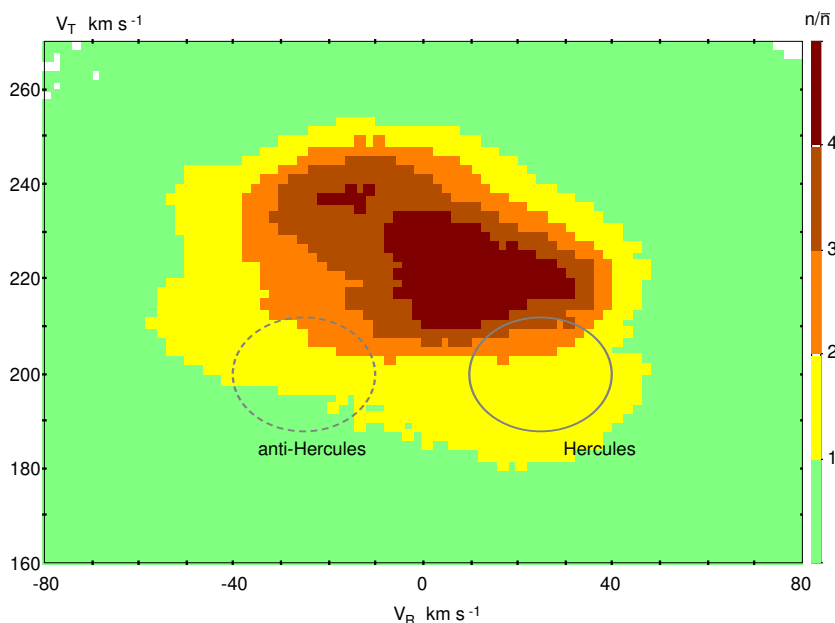


Fig. 1. Distribution of Gaia DR3 stars on the (V_R, V_T) plane. The color shows the ratio of the number of stars in $2 \times 2 \text{ km s}^{-1}$ areas to the average number of stars in the areas containing at least 10 stars (see the color palette on the right). We consider stars located at the distance $r < 0.5$ kpc from the Sun, near the Galactic plane, $|z| < 200$ pc, with the parallax to parallax error ratio $\varpi/\varepsilon_\varpi > 5$, the error of RUWE < 1.4 , the vertical velocity $|V_z| < 50 \text{ km s}^{-1}$, and the line-of-sight velocity measured by the Gaia spectrometer. The positions of the Hercules and anti-Hercules regions are shown by ellipses centered at $V_R = 25$ and $V_T = 200 \text{ km s}^{-1}$ (Hercules, solid line), and at $V_R = -25$ and $V_T = 200 \text{ km s}^{-1}$ (anti-Hercules, dotted line), with semi-axes of $\Delta V_R = 15$ and $\Delta V_T = 12 \text{ km s}^{-1}$.

s^{-1} , respectively. It is evident that the Hercules region includes the greatest number of model stars at the time period $t = 2.5\text{--}2.6$ Gyr from the start of simulation (Fig. 2d).

Hereinafter, we will also consider the anti-Hercules region which is needed for comparison between the model and observations. The Hercules and anti-Hercules regions are located symmetrically relative to the vertical axis $V_R = 0$. The strict definition of the Hercules and anti-Hercules regions/streams is as follows: a star belongs to the Hercules or anti-Hercules region/stream if it passes within 0.5 kpc of the Sun during the period considered and its velocities V_R and V_T lie within the ellipse centered at $V_R = 25$ and $V_T = 200 \text{ km s}^{-1}$ (Hercules), or at $V_R = -25$ and $V_T = 200$ (anti-Hercules), with semi-axes $\Delta V_R = 15$ and $\Delta V_T = 12 \text{ km s}^{-1}$ (Fig. 2d).

4.2 Variations in the number of stars in the Hercules and anti-Hercules regions over time

We calculated the numbers of model stars in the Hercules, N_H , and anti-Hercules, N_{aH} , regions over the time period 0–6 Gyr. Each of the 60 values of N_H and N_{aH} represents the sum of the instantaneous star numbers obtained for 10 moments separated by 10 Myr. Fig. 3a shows that the star number in the Hercules region (N_H , red line) reaches the first maximum at the interval 2.0–2.6 Gyr, then decreases. The second max-

imum N_H occurs during the period 4.3–5.2 Gyr and looks more like a plateau. The number of stars in the anti-Hercules region (N_{aH} , blue line) shows well-defined oscillations with a period of $P = 1.8 \pm 0.1$ Gyr. We previously observed a change in the number of stars in some regions with the period close to $P \approx 2.0$ Gyr, which is caused by librations of orbits near the OLR (Melnik, Podzolkova, and Dambis, 2023; Melnik and Podzolkova, 2024). Note that the maximum in the distribution of N_H (red line) at the time period $t = 2.0\text{--}2.6$ Gyr coincides with the minimum in the distribution of N_{aH} (blue line).

Fig. 3b shows variations of the relative difference f in the number of stars in the Hercules and anti-Hercules regions:

$$f = 2 \frac{N_H - N_{aH}}{N_H + N_{aH}}, \quad (1)$$

which does not depend on the number of stars neither in the model nor observational samples.

Fig. 3b also shows the observational value of f (dashed line) calculated for Gaia DR3 stars located in the region $r < 0.5$ and $|z| < 0.2$ kpc and in the ellipses on the (V_R, V_T) plane corresponding to the Hercules and anti-Hercules regions. The observational value of f is $f_g = 0.315 \pm 0.004$. For model stars, minimum and maximum values of f are -0.009 and 0.656 , respectively, with an average value of $\bar{f} = 0.291 \pm 0.011$

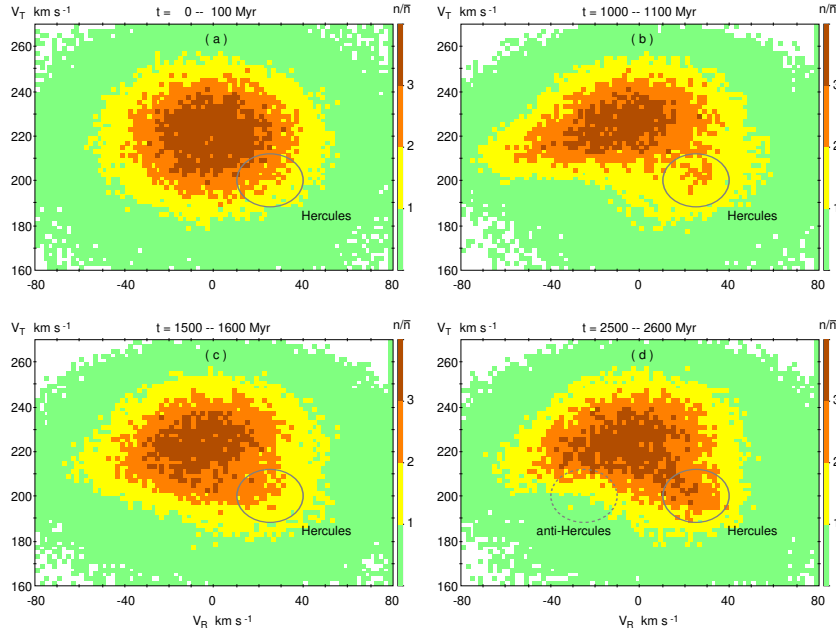


Fig. 2. Distribution of model stars located at the distance of $r < 0.5$ kpc from the Sun on the (V_R, V_T) plane at the different time periods. We calculated the number of stars n in areas of 2×2 km s $^{-1}$ in size and compared them with the average number of stars, \bar{n} , in similar areas containing at least one star, $n \geq 1$, in the region of $-80 < V_R < 80$ and $160 < V_T < 270$ km s $^{-1}$. As the ratio n/\bar{n} increases, the color of the area changes from green to brown (see the color palette on the right). The position of the Hercules region is shown by the ellipse with the center at $V_R = 25$ and $V_T = 200$ km s $^{-1}$ and the semi-axes of $\Delta V_R = 15$ and $\Delta V_T = 12$ km s $^{-1}$, respectively. It is clearly seen that the Hercules region includes maximum number of stars at the time period close to $t = 2500$ Myr from the start of simulation. Frame (d) also shows the position of the anti-Hercules region (dotted line), which is needed for calibration.

obtained over the time interval 0–6 Gyr. Thus, the observational value of f_g calculated for Gaia DR3 stars and the average value of f obtained for model stars are consistent within 1.6σ . A comparison of the model and observational values of f shows that there are many time moments when they coincide.

However, the observational value of f_g might be significantly underestimated. The sample of Gaia stars in the vicinity of $r < 0.5$ kpc from the Sun contains a noticeable number of thick-disk and halo stars, even inside the layer $|z| < 200$ pc. Suppose that the velocity distribution of thick-disk and halo stars in the region of $r < 0.5$ kpc is symmetric relative to the line $V_R = 0$. In this case, the numerator in Eq. 1 would not be affected by selection effects, since the number of thick-disk and halo stars in the Hercules and anti-Hercules regions must be approximately the same. However, the denominator in Eq. 1 must include twice the number of thick-disk and halo stars. Therefore, the value of f_g calculated solely for thin-disk stars can be noticeably higher than the value of $f_g = 0.315$ obtained here. In addition, selection effects related to the choice of the brightest stars for line-of-sight velocity measurements in crowded regions also lead to an underestimation of the f_g value (see Section 4.7).

4.3 Orientation of orbits in the Hercules and anti-Hercules regions

Fig. 4a shows the distribution of model stars on the (V_R, V_T) plane. We consider only stars that fall within the vicinity of $r < 0.5$ kpc from the Sun at the time period $t = 2.5$ – 2.6 Gyr from the start of simulation. We divided model stars into three groups depending on orientation of their orbits: elliptical orbits, i.e. orbits with the order of symmetry $n_s = 2$, elongated perpendicular to the bar ($75 \leq \theta_{00} < 105^\circ$); elliptical orbits ($n_s = 2$) elongated parallel to the bar ($0 \leq \theta_{00} < 15^\circ$ or $165 \leq \theta_{00} < 180^\circ$); and other orbits. The angle θ_{00} determines the average orientation of the orbit relative to the major axis of the bar at the time period $t = 0$ – 3 Gyr from the start of simulation. To avoid overloading the Figure with objects, we show only 2% of stars. The boundaries of the Hercules and anti-Hercules regions are also outlined. It is clearly seen that the majority of stars in the Hercules region have orbits elongated perpendicular to the bar while in the anti-Hercules region orbits are stretched parallel to the bar.

Fig. 4b shows the most probable orientation of orbits in different regions of the (V_R, V_T) plane. We divided the (V_R, V_T) plane in the range of values $-80 < V_R < 80$ and $160 < V_T < 270$ km s $^{-1}$ into 2×2 km s $^{-1}$ areas. For each area, we calculated the number of stars, n_\perp ,

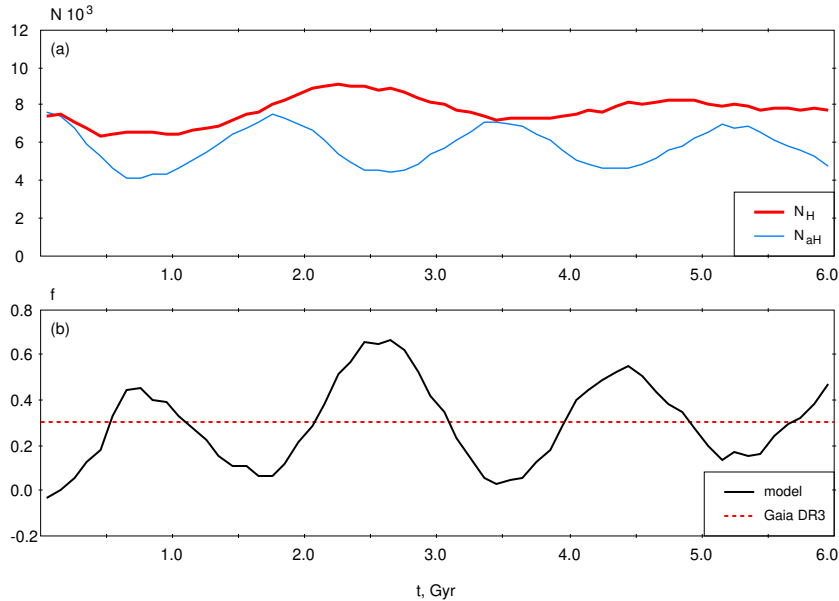


Fig. 3. (a) Variations in the number of model stars in the Hercules region (N_H , red line) and in the anti-Hercules region (N_{aH} , blue line). (b) Variations in the relative difference, f , of stars in the Hercules and anti-Hercules regions (Eq. 1) over time calculated for model stars (black curve) and for Gaia DR3 stars ($f_g = 0.315$, red dashed line).

whose orbits have an elliptical shape ($n_s = 2$) and are stretched perpendicular to the bar ($75 \leq \theta_{00} < 105^\circ$); the number of stars, n_{\parallel} , whose orbits have an elliptical shape ($n_s = 2$) and are elongated parallel to the bar ($0 \leq \theta_{00} < 15^\circ$ or $165 \leq \theta_{00} < 180^\circ$); and the number of stars, n_{oth} , with a different value of n_s ($n_s \neq 2$) or a different orbital orientation. If most stars in the area have elliptical orbits elongated perpendicular to the bar ($n_{\perp} > n_{\parallel}$ and $n_{\perp} > n_{oth}$), the area is shown in red; if most stars have elliptical orbits elongated parallel to the bar ($n_{\parallel} > n_{\perp}$ and $n_{\parallel} > n_{oth}$), then it is shown in blue; and if most orbits have a different order of symmetry or a different orientation ($n_{oth} > n_{\perp}$ and $n_{oth} > n_{\parallel}$), then the area is shown in gray. It is clearly seen that the majority of stars in the Hercules and anti-Hercules regions have elliptical orbits elongated perpendicular and parallel to the bar, respectively.

Fig. 5 shows the distributions of elliptical orbits along the angle θ_{00} in the Hercules and anti-Hercules regions. The fraction of elliptical orbits ($n_s = 2$) in these regions reaches 85% and 87%, respectively. Fig. 5 shows that almost all stars (84%) in the Hercules region have orbits elongated perpendicular to the bar ($75 \leq \theta_0 < 105^\circ$). In contrast, in the anti-Hercules region most stars have orbits elongated parallel to the bar: 54% are oriented at the angle θ_{00} in the range of $165 \leq \theta_{00} < 180^\circ$ and 14% at the angle θ_{00} in the range of $0 \leq \theta_{00} \leq 15^\circ$; and only 18% are elongated perpendicular to the bar ($75 \leq \theta_{00} < 105^\circ$).

Among all model stars that fall in the solar neighborhood, $r < 0.5$ kpc, at the time period of $t = 2.5$ – 2.6

Gyr, 21% have elliptical orbits ($n_s = 2$) elongated perpendicular to the bar ($75 \leq \theta_{00} < 105^\circ$), and 19% have elliptical orbits ($n_s = 2$) elongated parallel to the bar ($0 \leq \theta_{00} < 15^\circ$ or $165 \leq \theta_0 < 180^\circ$). Moreover, in the latter case, 11% have orbits oriented at the angle of θ_{00} in the range of $0 \leq \theta_{00} < 15^\circ$ and 8% in the range of $165 \leq \theta_{00} < 180^\circ$. Thus, the distribution of orbits along the angle θ_{00} in the Hercules and anti-Hercules regions differs significantly from the general distribution of stars in the vicinity of the Sun.

4.4 Initial values of R , V_T and V_R in the Hercules and anti-Hercules regions

Fig. 6 shows the distributions of the numbers of model stars N in the Hercules and anti-Hercules regions along the initial value of the Galactocentric distance $R(0)$. The bin width along $R(0)$ is 250 pc. We consider model stars that fall in the solar neighborhood, $r < 0.5$ kpc, at the time period $t = 2.5$ – 2.6 Gyr. The median values of the initial distances R in the Hercules and anti-Hercules regions are 6.8 and 7.3 kpc, respectively, i. e. most stars arrive in the Hercules (anti-Hercules) region from distances smaller (larger) than the OLR radius ($R_{OLR} = 7.0$ kpc).

Fig. 6a and Fig. 6c also show the median values of the initial azimuthal velocity $V_T(0)$ and the $+/-$ dispersion in V_T calculated in each bin along $R(0)$. The general tendency is clearly visible: a decrease in the value of V_T with increasing R , although there is a small plateau (7.0–8.0 kpc) in the Hercules region. The decrease in the initial value of V_T with increasing R may be due

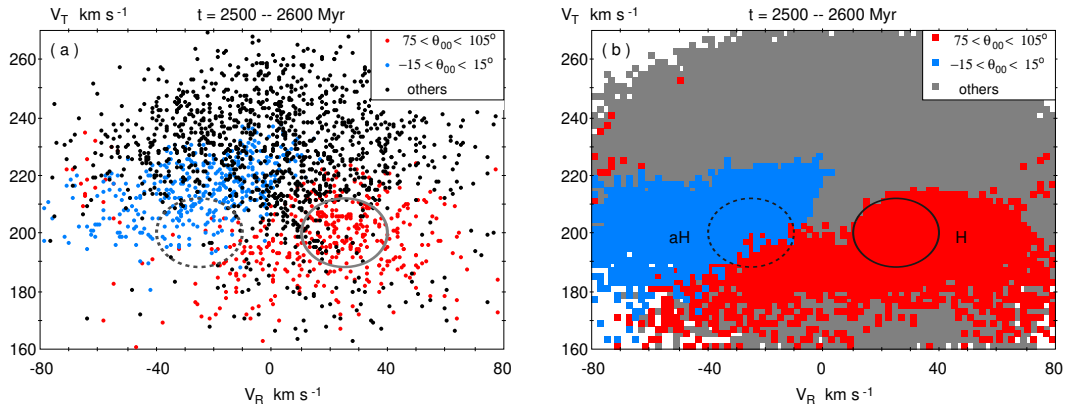


Fig. 4. (a) Distribution of model stars on the (V_R, V_T) plane and their orbital orientation relative to the bar. Stars with elliptical orbits elongated perpendicular to the bar ($75 \leq \theta_{00} < 105^\circ$) are shown in red; stars with elliptical orbits ($n_s = 2$) elongated parallel to the bar ($0 \leq \theta_{00} < 15^\circ \cup 165 \leq \theta_{00} < 180^\circ$) are shown in blue; all other cases are shown in gray. The angle θ_{00} determines the average orientation of the orbit relative to the major axis of the bar at the time period 0–3 Gyr. 2% of stars are represented. We consider model stars that fall in the neighborhood of the Sun, $r < 0.5$ kpc, at the time period of $t = 2.5$ –2.6 Gyr. Also shown the boundaries of the Hercules (solid line) and anti-Hercules (dashed line) regions. (b) Distribution of areas of 2×2 km s $^{-1}$ in size on the (V_R, V_T) plane, the color of which shows the most probable orientation of the orbits. The areas in which the majority of stars have elliptical orbits ($n_s = 2$) elongated perpendicular to the bar ($75 \leq \theta_{00} < 105^\circ$) are shown in red; the areas in which most of stars have elliptical orbits ($n_s = 2$) elongated parallel to the bar ($0 \leq \theta_{00} < 15^\circ \cup 165 \leq \theta_{00} < 180^\circ$) are shown in blue; areas in which most of stars have another orientation of orbits or a different order of symmetry are shown in gray. It is clearly seen that the majority of stars in the Hercules and anti-Hercules regions have elliptical orbits elongated perpendicular and parallel to the bar, respectively.

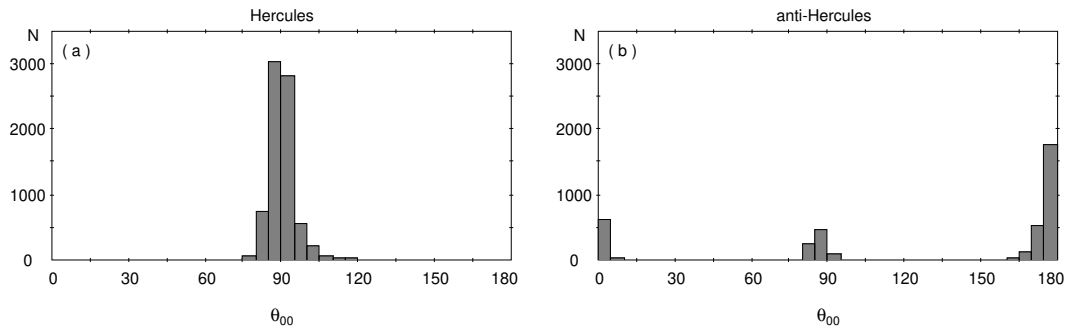


Fig. 5. Distributions of elliptical orbits ($n_s = 2$) along the angle θ_{00} in the (a) Hercules and (b) anti-Hercules regions. The angle θ_{00} lies in the range $0 \leq \theta_{00} < 180^\circ$ and determines the average orientation of the orbit relative to the major axis of the bar at the time period $t = 0$ –3 Gyr. We consider model stars which fall in the solar neighborhood, $r < 0.5$ kpc, at the time period of $t = 2.5$ –2.6 Gyr. It is clearly seen that most stars in the Hercules region have orbits elongated perpendicular to the bar ($75 \leq \theta_{00} < 105^\circ$) while those in the anti-Hercules region have orbits elongated parallel to the bar, specifically at the angle θ_{00} in the range $165 \leq \theta_{00} < 180^\circ$.

to highly elongated orbits. In order a star to reach quickly the OLR radius from the initial distance R less (greater) than $R_{OLR} = 7.0$ kpc, it must have a greater (lower) azimuthal velocity than stars have, on average, at this distance.

Fig. 6b and Fig. 6d show the median values of the initial radial velocity $V_R(0)$ and the $+/-$ dispersion in V_R . The median radial velocities $V_R(0)$ in the Hercules region vary in the range $[-2, 8]$ km s $^{-1}$. Interestingly, the median radial velocity in the bin $R(0) = 7.00-7.25$ kpc, corresponding to maximum number of stars N is $V_R(0) \approx 0$. This is due to the fact that the most probable value of the initial radial velocity is zero, $V_R(0) = 0$, so there are a lot of such stars in the model.

As for the anti-Hercules region (Fig. 6d), here the median value of the initial velocity $V_R(0)$ sharply decreases from 25 to 3 km s $^{-1}$ at the interval 6.0–7.5 kpc and fluctuates in the range $[-5, 3]$ km s $^{-1}$ at the interval 7.5–8.5 kpc. Once again, we observe that the bins with maximum number of particles N correspond to $V_R(0) \approx 0$.

The dispersion of the initial azimuthal velocities in the Hercules and anti-Hercules regions is $\sigma_T \approx 20$ km s $^{-1}$, which is close to the dispersion of the stellar velocities at the distance of R_0 . The dispersion of the initial radial velocities in the Hercules region is $\sigma_R \approx 30$ km s $^{-1}$, which is also close to the dispersion of the radial velocities in the surrounding disk. In the anti-Hercules region, the dispersion of the initial radial velocities is noticeably larger, $\sigma_R \approx 38$ km s $^{-1}$, which is possibly due to orbital libration.

4.5 Orbits in the Hercules and anti-Hercules regions

Fig. 7 shows typical stellar orbits in the Hercules (upper row) and anti-Hercules (lower row) regions. The Galaxy rotates counterclockwise. The orbits are considered in the reference frame of the rotating bar. All stars considered are located outside the Corotation Radius of the bar ($R > R_{CR}$), so in the bar reference frame they rotate in the sense opposite that of the Galactic rotation, i. e. clockwise. The supposed position of the Sun relative to the bar and the initial position of the star are shown by the yellow and black circles, respectively. The initial values of the distances, $R(0)$, radial, $V_R(0)$, and azimuthal, $V_T(0)$, velocities of the stars are given at the top of each frame. The segments of the orbits at the time intervals 0–1, 1–2 and 2–3 Gyr are shown in green, red and blue, respectively. For each orbit, we give the angle θ_{00} , which determines the average orientation of the orbit relative to the major axis of the bar at the time interval 0–3 Gyr. We will also consider the angle θ_0 characterizing the orientation of the orbit relative to the major axis of the bar at the time interval of one radial oscillation of a star (from one intersection of the average radius of the orbit with a negative ra-

dial velocity to another). For each star, we present the period P of variations in the angular momentum and total energy, as well as the Jacobi energy E_J , which is conserved after the bar reaches its full power.

Fig. 8 (left panel) shows oscillations of the angular momentum L of the stars A , B , C , and D , whose orbits are shown in frames (a), (b), (c), and (d) of Fig. 7, respectively. The fast and slow oscillations of L are clearly visible. The fast oscillations with a period of $P = 0.13$ Gyr occur twice during one period of the star's revolution relative to the bar. The slow oscillations result from the beats between the frequency with which a star encounters perturbations from the bar, $2(\Omega - \Omega_b)$, and the epicyclic frequency, κ (for more details, see Melnik, Podzolkova, and Dambis, 2023; Melnik and Podzolkova, 2024). The periods of slow oscillations in L of stars A , B , C , and D are $P = 0.94, 2.65, 1.92,$ and 1.93 Gyr, respectively.

Fig. 8 (right panel) shows oscillations of the angle θ_0 characterizing the direction of orbit elongation at the time interval of one radial oscillation. Frames (A), (B), (C), and (D) correspond to the stellar orbits shown in frames (a), (b), (c), and (d) of Fig. 7. It is clearly seen that the periods P of slow variations in the angular momentum L coincide with the periods of variations in the direction of the orbit elongation. Note that the eccentricity and average radius of orbits also change with the period P (see, for example, Melnik, Podzolkova, and Dambis, 2023, Fig. 11).

Fig. 7a shows a typical orbit of a star in the Hercules region. The initial distance is $R(0) = 6.8$ kpc, which is less than the OLR radius ($R_{OLR} = 7.0$ kpc), and the initial azimuthal velocity is $V_T(0) = 216$ km s $^{-1}$, which is slightly less than the most probable value (218 km s $^{-1}$) of the initial azimuthal velocity at this distance. The initial radial velocity is $V_R(0) = 10$ km s $^{-1}$. A small positive radial velocity is needed for the orbit to be elongated enough to bring the star into the solar vicinity of $r < 0.5$ kpc. It is clearly seen that the orbit changes with time, but it always lies inside the figure bounded by two ellipses elongated perpendicular to the bar. The average value of the angle θ_{00} is $\theta_{00} = 90^\circ$.

Fig. 8A shows the change in the direction of elongation of the star's orbit (Fig. 7a) over time. We can clearly see that the angle θ_0 increases almost linearly from the value -90 to 90° , and then a new revolution begins. The values of $\theta_0 = \pm 90^\circ$ correspond to the same orientation of the elliptical orbit. The change in the direction of the orbit elongation of the star A occurs only in the direction of increasing θ_0 . Thus, here we are not dealing with oscillations of orbit orientation but with the rotation of the direction of orbit elongation in one sense. In the case considered, the orbit rotates in the positive sense, i. e. in the sense of the Galactic rotation. Note that the rotation velocity of the orbit

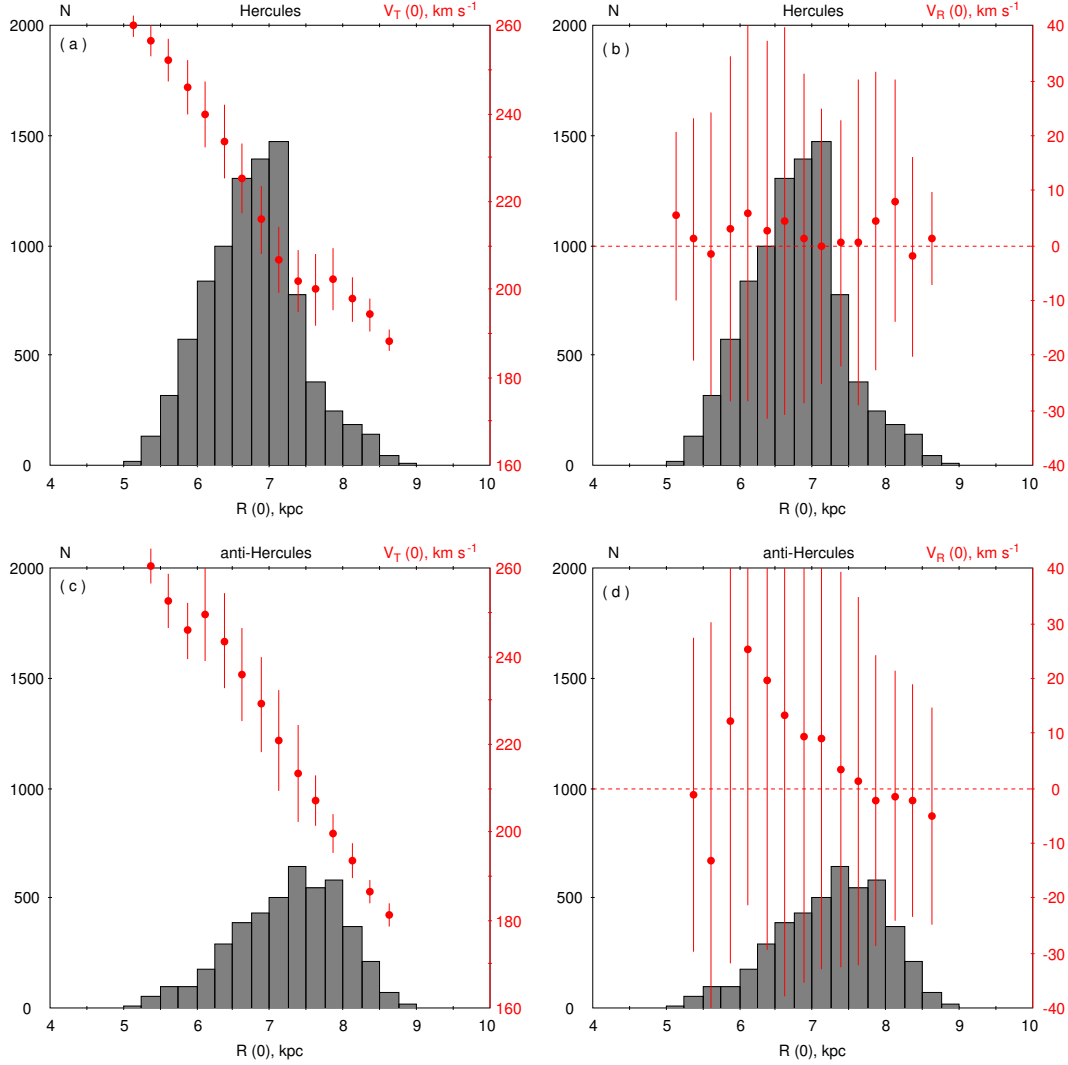


Fig. 6. Distributions of the numbers of model stars N along the initial value of the distance $R(0)$ (gray bars) in the (a, b) Hercules and (c, d) anti-Hercules regions. Other distributions are superimposed upon these histograms: (a, c) the median values of the initial azimuthal velocity $V_T(0)$ and (b, d) the median values of the initial radial velocity $V_R(0)$ (red circles) calculated in each bin along R . The red vertical lines show the \pm dispersion of the median velocities. The scales of variations in the V_T and V_R velocities are shown on the right vertical axes. We can clearly see the general tendency for the V_T -variations: a decrease in the value of $V_T(0)$ with increasing $R(0)$, although there is a small plateau (7.0–8.0 kpc) in the Hercules region. The median radial velocity $V_R(0)$ in the Hercules region fluctuates in the range $[-2, 8]$ km s^{-1} while in the anti-Hercules region the velocity $V_R(0)$ sharply decreases from 25 to 3 km s^{-1} at the interval 6.0–7.5 kpc and fluctuates in the range $[-5, 3]$ km s^{-1} at the interval 7.5–8.5 kpc. In general, the bins along R containing maximum number of stars correspond to nearly zero value of the initial radial velocity, $V_R(0)$. We consider model stars which fall in the solar vicinity, $r < 0.5$ kpc, at the time period $t = 2.5\text{--}2.6$ Gyr.

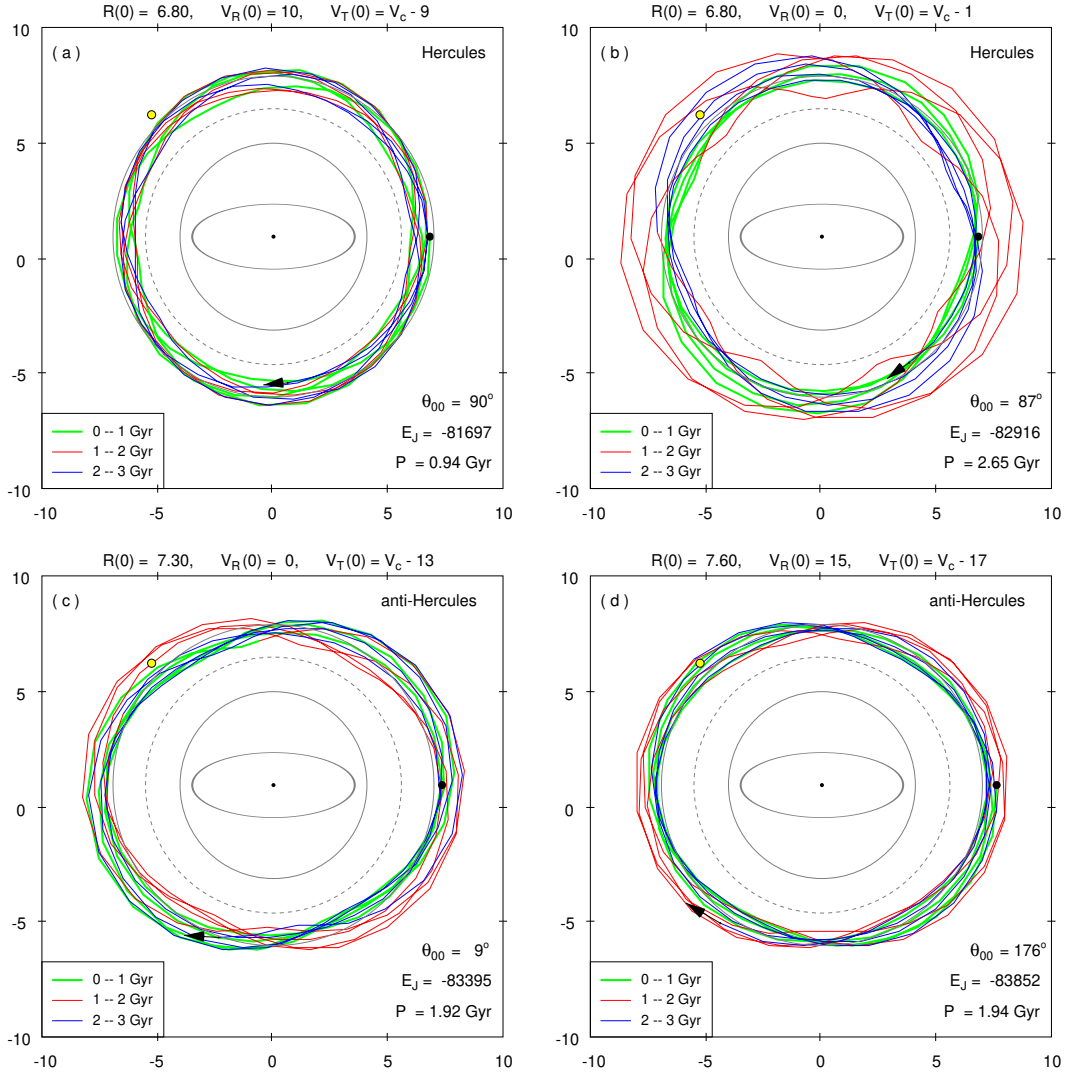


Fig. 7. Typical orbits of stars in the Hercules (top row) and anti-Hercules (bottom row) regions. The orbits are shown in the bar reference frame, in which stars considered rotate in the direction opposite that of the Galactic rotation. The supposed position of the Sun and the initial position of the star are shown by the yellow and black circles, respectively. The initial values of the distances, $R(0)$, radial, $V_R(0)$, and azimuthal, $V_T(0)$, velocities of the stars are given at the top of each frame. The segments of the orbits outlined by the stars at the time intervals 0–1, 1–2 and 2–3 Gyr are shown in green, red and blue, respectively. For each orbit, we list the angle θ_{00} , which characterizes the average orientation of the orbit relative to the major axis of the bar at the time interval 0–3 Gyr, the Jacobi energy E_J , and the period P of variations in the angular momentum. The values of distances, velocities and E_J are given in units of kpc, km s^{-1} and $\text{km}^2 \text{s}^{-2}$, respectively. Also are shown the positions of the bar (ellipse), CR and OLR (solid gray lines), and $-4/1$ resonance (gray dashed line). It is clearly seen that the orbits in the Hercules region are, on average, elongated perpendicular to the bar while the orbits in the anti-Hercules region are oriented parallel to the bar.

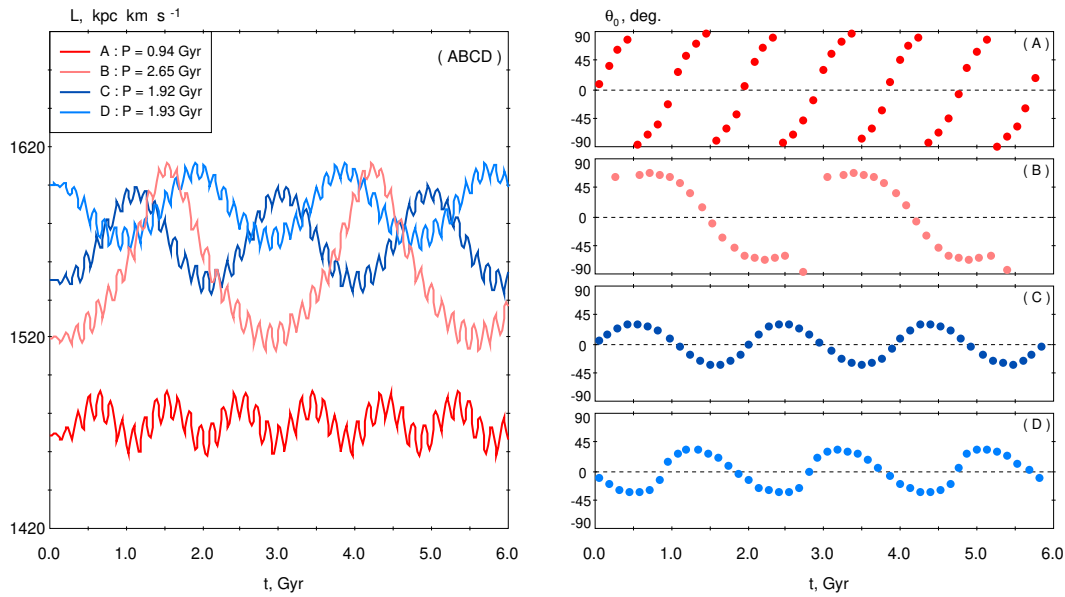


Fig. 8. (Left panel) Oscillations of the angular momentum L of the stars A, B, C, and D, whose orbits are shown in frames (a), (b), (c), and (d) of Fig. 7, respectively. We can clearly see the fast and slow oscillations of L . The periods of the slow oscillations of L for stars A, B, C, and D are 0.94, 2.65, 1.92, and 1.93 Gyr, respectively. (Right panel) Oscillations of the angle θ_0 , which characterizes the direction of orbit elongation at the time interval of one radial oscillation of the star. It is clearly seen that in frame (A) the angle θ_0 only increases while it oscillates in frames (B), (C), and (D).

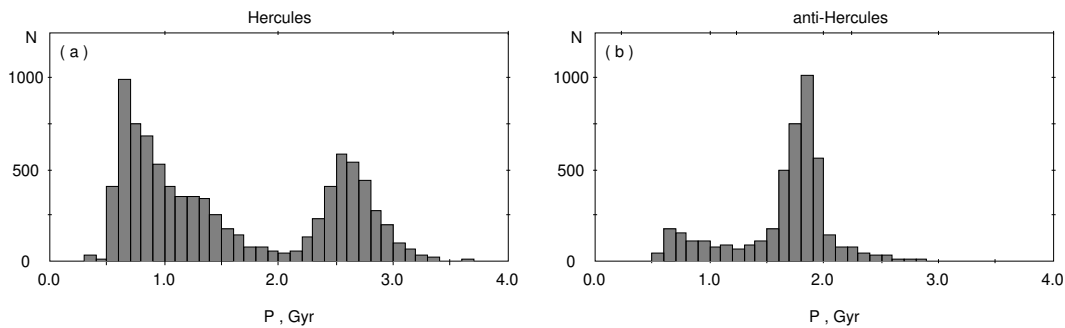


Fig. 9. Distribution of orbits along the period P of slow variations in the angular momentum in the (a) Hercules and (b) anti-Hercules regions. It is clearly seen that in the Hercules region, the distribution has two maxima located at $P = 0.7$ and 2.6 Gyr while in the anti-Hercules region, the maximum corresponds to $P = 1.9$ Gyr.

increases slightly when the orbit is oriented parallel to the bar ($\theta_0 \approx 0^\circ$).

Fig. 7b shows another typical orbit in the Hercules region. The initial values of the distance and azimuthal velocity of the star considered are $R(0) = 6.8$ kpc and $V_T(0) = 224$ km s $^{-1}$. It is clearly seen that the direction of orbit elongation changes from $\theta_0 = \pm 90^\circ$ (elongated perpendicular to the bar) to $\theta_0 = 0^\circ$ (elongated parallel to the bar). The angle θ_{00} , which determines the average orientation of the orbit, is $\theta_0 = 87^\circ$, because most of the time at the interval 0–3 Gyr the orbit is elongated perpendicular to the bar. Fig. 8B shows that oscillations of the angle θ_0 are not sinusoidal. We can see a sharp jump from the value $\theta_0 = -90^\circ$ to 60° , then θ_0 decreases sinusoidally to -60° , after which there is a rapid rearrangement of the orbit: first the value θ_0 drops to -90° , then sharply increases to $\theta_0 = 60^\circ$. Note that the Galactocentric distance R to the star varies in a very wide range, $R = 6.0$ – 8.8 kpc, i.e. the star comes very close to the resonance $-4/1$ ($R_{-4/1} = 5.5$ kpc) in the inner region and goes to distances exceeding the OLR radius ($R_{OLR} = 7.0$ kpc) by 1.8 kpc in the outer region. In general, we view an orbit with a wide range of the distance R variation.

Possibly, it is these orbits (Fig. 7b) that increase the number of stars N_H in the Hercules region at the period 2–3 Gyr (Fig. 3a). It is clearly seen that the angle θ_0 at the time interval of 1.8–2.6 Gyr has a value close to $\theta_0 \approx -60^\circ$ (Fig. 8B). In this case, the orbit is tilted to the left (in the sense of the Galactic rotation) relative to the minor axis of the bar and lies near the Sun (Fig. 7b, blue line), besides, the star passes the Sun with a positive radial velocity, and, consequently, can fall inside the Hercules region on the (V_R , V_T) plane. In other time intervals, this star does not fall into the solar neighborhood, $r < 0.5$ kpc, with a positive radial velocity ($10 < V_R < 40$ km s $^{-1}$): at the time period 0.5–1.3 Gyr, its orbit is inclined to the right relative to the minor axis of the bar (Fig. 7b, green line) and lies at a large distance from the Sun while at the time period 1.3–1.8 Gyr, its orbit is stretched almost parallel to the bar ($\theta_0 \approx 0^\circ$) and the star flies near the Sun with a negative radial velocity (Fig. 7b, red line).

Fig. 7c shows a typical orbit of a star in the anti-Hercules region. The initial values of the distance and azimuthal velocity are $R(0) = 7.3$ kpc and $V_T(0) = 212$ km s $^{-1}$. It is clearly seen that the orbit is elongated, on average, almost parallel to the bar, the angle θ_{00} is $\theta_{00} = 9^\circ$. The fact that the value θ_{00} is not exactly zero, $\theta_{00} \neq 0^\circ$, is due to the circumstance that most of the time during the interval 0–3 Gyr, this orbit is tilted to the right relative to the minor axis of the bar. The direction of orbit elongation oscillates almost sinusoidally from -45° to 45° with the period $P = 1.92$ Gyr (Fig. 8C). In our

previous works, we showed that oscillations of such orbits cause the periodic change in the morphology of the outer rings and the appearance of humps on the profiles of the V_R -velocity distribution along the distance R (Melnik, Podzolkova, and Dambis, 2023; Melnik and Podzolkova, 2024).

Fig. 7d shows another orbit of a star in the anti-Hercules region. The initial values of the distance and azimuthal velocity are $R(0) = 8.0$ kpc and $V_T(0) = 200$ km s $^{-1}$. The angle θ_{00} is $\theta_{00} = 176^\circ$, i. e. the orbit is tilted to the left relative to the minor axis of the bar most of the time at the interval 0–3 Gyr. It is clearly seen that the angle θ_0 slowly decreases from 45° to -45° and then quickly grows back to 45° (Fig. 8D).

A comparison of Fig. 8C and Fig. 8D, as well as Fig. 7c and Fig. 7d, shows that oscillations in the direction of orbit elongation of the stars C and D occur practically in antiphase.

In general, the orbits of stars in the Hercules region (Fig. 7a and Fig. 7b) support the outer ring R_1 elongated perpendicular to the bar, while in the anti-Hercules region (Fig. 7c and Fig. 7d) – the ring R_2 elongated parallel to the bar.

The eccentricities of the orbits shown in Fig. 7 also vary with the periods equal to the periods of slow variations in the angular momentum of the stars. The ranges of variations in the eccentricities of the stars A , B , C , and D are (a) 0.38–0.58, (b) 0.44–0.73, (c) 0.43–0.70, and (d) 0.30–0.62, respectively. Thus, the stars B and C have more elongated orbits than stars A and D .

4.6 Distribution of orbits along the period P in the Hercules and anti-Hercules regions

Fig. 9 shows the distribution of orbits along the period P of slow variations in the angular momentum in the (a) Hercules and (b) anti-Hercules regions. It is clearly seen that in the Hercules region, the distribution has two maxima corresponding to the periods $P = 0.7$ and 2.6 Gyr. The first maximum ($P = 0.7$ Gyr) is created by orbits that always lie inside the figure bounded by two ellipses stretched perpendicular to the bar (Fig. 7a), therefore, these orbits are, on average, stretched perpendicular to the bar, and stars on them spend most of their time inside the OLR radius, $R \leq R_{OLR}$. The second maximum ($P = 2.6$ Gyr) is created by orbits that are most of the time elongated at the angles $\theta_0 \approx 60^\circ$ or $\theta_0 \approx -60^\circ$ to the major axis of the bar, and a small part of their time – parallel to the bar (Fig. 7b). In addition, these orbits are characterized by a large range of variation in the distance R , $\Delta R > 2.5$ kpc. In this case, stars are located both inside and outside the OLR radius approximately half of the time.

Fig. 9b shows that the maximum of the orbit distribution along the period P in the anti-Hercules region

corresponds to $P = 1.9$ Gyr. This period coincides with the most probable value of the period of the angular momentum variations of stars on librating orbits near the OLR (Melnik and Podzolkova, 2024). Thus, most orbits in the anti-Hercules region are expected to librate relative to the major axis of the bar.

4.7 Comparison with the Gaia DR3 data

The study of model-star samples has shown that at the initial time, stars in the Hercules region are, on average, slightly closer to the Galactic center than stars in the anti-Hercules region (Section 4.4). If the Galactic disk formed inside-out (e. g., Chiappini, Matteucci, and Romano, 2001) then we can expect that stars in the Hercules region must be, on average, older and redder than stars in the anti-Hercules region. Here we use the fact that most of stars in the Gaia catalog lie on the main sequence of the Hertzsprung-Russell diagram (Babusiaux et al., 2018). This hypothesis would be correct if the overwhelming majority of stars in the solar neighborhood were formed before the epoch of the bar formation, but recent episodes of star formation can alter the distribution of stellar ages in these regions. In addition, selection effects depend not only on the value of the magnitude G and color, but also on the direction to a star. In crowded areas of the sky, the processing program automatically selects brighter objects (e.g., Boubert and Everall, 2020).

Table 1 presents the median values of the magnitude, G , color, $G - G_{RP}$, and absolute magnitude, M_G , of stars in the Hercules and anti-Hercules regions derived from the Gaia DR3 data. It also provides their uncertainties and the number of stars with known values of the corresponding parameters. The absolute magnitudes M_G were calculated without taking into account the extinction, which must be small in the vicinity of 0.5 kpc from the Sun:

$$M_G = G - 5 \log_{10} r - 10, \quad (2)$$

where r is the heliocentric distance in units of kpc. We use the $G - G_{RP}$ values because they are more accurate than $G_{BP} - G_{RP}$ and are measured for a larger number of stars (Andrae et al., 2018; Vallenari et al., 2023).

Table 1 shows that the Hercules region includes slightly brighter, bluer, and more luminous stars than the anti-Hercules region. Although the differences in the median values do not exceed 0.14^m , their statistical significance (the ratio of the value to its uncertainty) exceeds 8σ .

Fig. 10a shows the distribution of the differences Δn between the number of Gaia DR3 stars in the Hercules region and the normalized number of stars in the anti-Hercules region, calculated in small areas on the Hertzsprung-Russell diagram. The horizontal axis

shows the color, $G - G_{RP}$, while the vertical axis indicates the absolute stellar magnitude M_G . The sizes of the areas are 0.026 and 0.157^m , respectively. Normalization to the number of stars is necessary, as the Hercules and anti-Hercules regions include the different numbers of stars. The normalization factor, $k = 1.37$, equals the ratio of the numbers of stars with known line-of-sight velocities, parallaxes, G and G_{RP} values in the Hercules and anti-Hercules regions. Areas in which the number of stars in the Hercules region exceeds (falls below) the normalized number of stars in the anti-Hercules region are shown in shades of red (green), respectively. The average value of the difference Δn is $|\overline{\Delta n}| \approx 7$. It is clearly seen that the part of the main sequence corresponding to the bluest and most luminous stars is colored red, indicating an excess of stars in the Hercules region compared to the anti-Hercules region in this part of the diagram. Note that the red giant branch is represented almost equally by both regions. Therefore, the Hercules region likely contains a larger fraction of relatively young stars than the anti-Hercules region. However, this result may also be due to selection effects: stars in the Hercules and anti-Hercules regions are distributed differently in space, although they are enclosed by the surfaces $r < 0.5$ and $|z| < 0.2$ kpc, which will be discussed below.

For completeness, we also compared the distributions of stars in the Hercules and Central regions (Fig. 10b). The Central region includes 361617 Gaia DR3 stars located in the solar neighborhood, $r < 0.5$ and $|z| < 0.2$ kpc, that satisfy the criterion $|V_z| < 50$ km s $^{-1}$, and lie on the (V_R, V_T) plane inside the ellipse centered at $V_R = 0$ and $V_T = 225$ km s $^{-1}$ with semi-axes $\Delta V_R = 15$ and $\Delta V_T = 12$ km s $^{-1}$. Since the velocity of the rotation curve at the solar distance is $V_c = 225$, the Central region contains a larger portion of stars with velocities close to that of the rotation curve, therefore, this region likely contains a higher proportion of young stars. In this case, the normalization factor is $k = 0.41$. It is clearly seen that the upper part of the main sequence is colored green, i.e. the Central region indeed contains relatively more blue stars than the Hercules region. On the other hand, the red giant branch is represented mainly by stars of the Hercules region. Consequently, the fraction of young stars in the Central region is indeed larger than in the Hercules region.

However, the differences in the distribution of stars in the Hercules and anti-Hercules regions on the Hertzsprung-Russell diagram may still be caused by selection effects. The selection function of Gaia DR3 stars into different samples, for example, into a sample of stars with known line-of-sight velocity, has a low value in the Galactic plane, and especially in the direction of the Galactic center. This indicates a lack of stars ($G < 21^m$) with measured line-of-sight velocity in

Table 1. Median G , $G - G_{RP}$ and M_G in the Hercules and anti-Hercules regions from the Gaia DR3 data

Hercules		anti-Hercules	
G			
13.4174 ± 0.0042^m	148403	13.4972 ± 0.0048^m	108002
$G - G_{RP}$			
0.6682 ± 0.0005^m	147903	0.6792 ± 0.0006^m	107656
M_G			
5.7723 ± 0.0045^m	148403	5.9110 ± 0.0054^m	108002

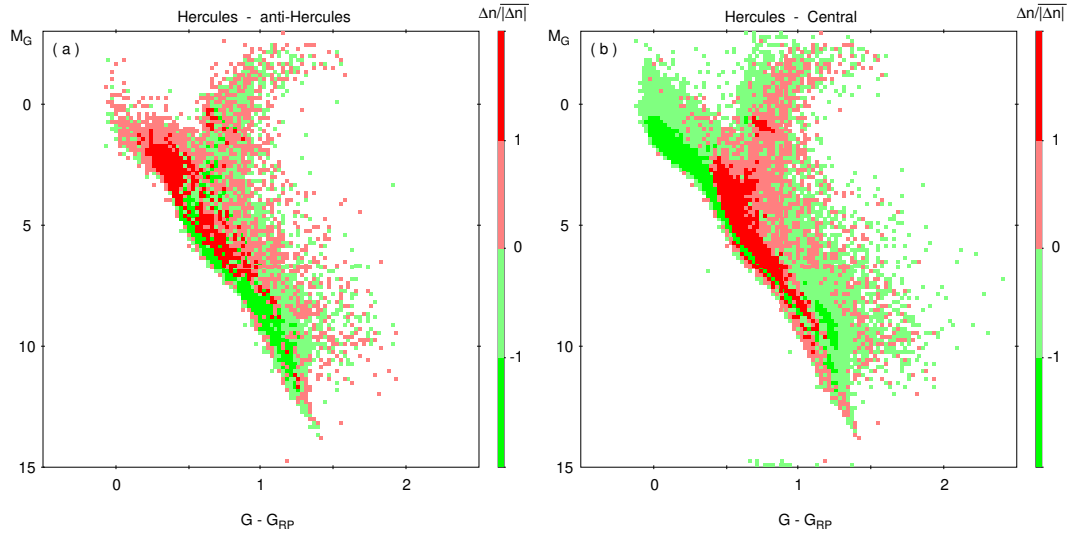


Fig. 10. Distribution of the differences Δn between the number of Gaia DR3 stars in the Hercules region and the normalized number of stars in (a) the anti-Hercules region and (b) the Central region on the Hertzsprung-Russell diagram. The horizontal axis shows the color, $G - G_{RP}$, and the vertical axis indicates the absolute stellar magnitude, M_G . The sizes of the areas are 0.026 and 0.157^m , respectively. Areas in which the number of stars in the Hercules region is greater (less) than the normalized number of stars in another region (namely, (a) the anti-Hercules region and (b) the Central region) are shown in shades of red (green). The average value of the difference Δn is $|\overline{\Delta n}| \approx 7$. The excess of stars in one region over the number of stars in another region by more than $|\overline{\Delta n}|$ is shown in bright red or green, respectively (see the color palette on the right). (a) It is clearly seen that the upper part of the main sequence corresponding to the bluest and most luminous stars is colored red indicating that the stars of the Hercules region predominate over those of the anti-Hercules region in this part of the diagram while the red giant branch is represented by both regions nearly equally. (b) The Central region includes relatively bluer and more luminous main-sequence stars than the Hercules region, and the red giant branch is represented mainly by stars of the Hercules region.

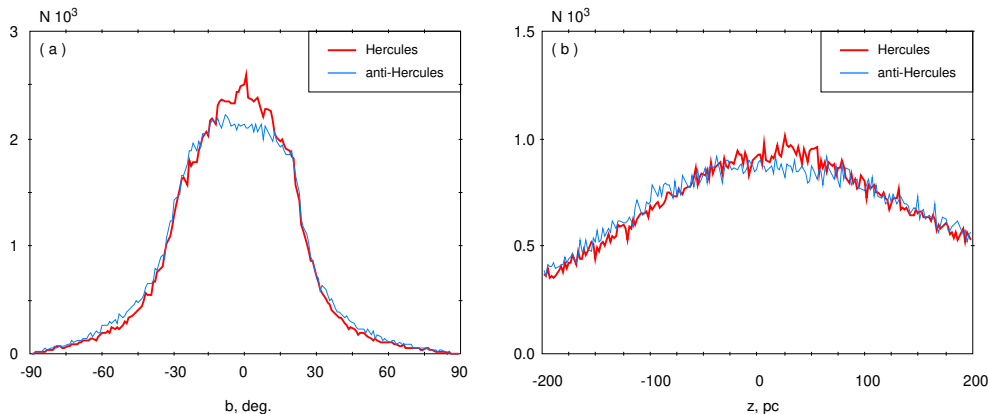


Fig. 11. Normalized distributions of the number of stars N in the Hercules (red line) and anti-Hercules (blue line) regions along (a) the Galactic latitude b and (b) the Galactic coordinate z . The width of the bins is (a) $\Delta b = 1^\circ$ and (b) $\Delta z = 2$ pc. (a) It is clearly seen that the Hercules region includes a significant excess of stars near the Galactic plane compared to the anti-Hercules region, which is, on average, 11% in the range $|b| < 10^\circ$ and reaches maximum value of 22% at $b = 0$. The distributions of stars in both regions are asymmetric with respect to the $b = 0$ line, and N drops much faster toward positive latitudes b . (b) We can also see the excess of stars of the Hercules region near the Galactic plane compared to the anti-Hercules one, which is, on average, 10% at the interval $z = 14$ –54 pc. Maximum value of N in the Hercules region corresponds to $z = 24$ pc. The distribution of stars in the anti-Hercules region has a broad maximum corresponding to the interval $z \in [-46, 66]$ pc.

these directions (Castro-Ginard et al., 2023). Since the Gaia DR3 stars in the Hercules and anti-Hercules regions are distributed differently in the sky, the influence of selection effects on these samples may be different.

Fig. 11a shows the distributions of the numbers of stars N in the Hercules and anti-Hercules regions as a function of the Galactic latitude b . Both distributions were normalized to the number of stars in the Hercules region, $N_H = 148404$, i.e. the number of stars in each sector in the anti-Hercules region was multiplied by the factor $k = 1.37$. The width of the sectors is $\Delta b = 1^\circ$. It is clearly seen that the Hercules region contains a significant excess of stars near the Galactic plane compared to the anti-Hercules region, which, on average, equals 11% in the range $|b| < 10^\circ$ and reaches maximum value of 22% at $b = 0$. Probably, the weaker concentration of stars of the anti-Hercules region toward the Galactic plane allowed the Gaia spectrometer to measure line-of-sight velocities for a larger fraction of faint stars in this region compared to the Hercules region. Thus, the number of stars in the anti-Hercules region N_{aH} was increased at the expense of faint stars, which decreased the relative abundance of bright stars in this sample. Note also that the distributions of stars in both regions are asymmetric with respect to the $b = 0$ line, and N decreases much faster in the direction of positive b values than in the opposite direction.

Fig. 11b shows the distributions of the numbers of stars N in the Hercules and anti-Hercules regions normalized to the number of stars in the Hercules region along the Galactic coordinate z . The bin width is $\Delta z = 2$ pc. To calculate z , we used the value of the solar coordinate z_\odot equal to $z_\odot = 27$ pc (Bland-Hawthorn and Gerhard, 2016). Here we also see an excess of stars of the Hercules region near the Galactic plane compared to the anti-Hercules region, which, on average, is 10% at the interval $z = 14$ –54 pc. Maximum value of the number of stars N in the Hercules region corresponds to $z = 24$ pc. The distribution of stars in the anti-Hercules region has a broad maximum corresponding to the interval $z \in [-46, 66]$ pc.

Fig. 12 shows the distributions of (a) the number of stars, N , (b) magnitude, G , (c) color, $G - G_{RP}$, and (d) absolute magnitude, M_G , of Gaia DR3 stars located in the Hercules and anti-Hercules regions, along the Galactic longitude l . For each longitude sector of the $\Delta l = 5^\circ$ width, we calculated the number of stars N within the sector, as well as the median values of G , $G - G_{RP}$ and M_G .

Fig. 12a shows the distribution of the number of stars N along the longitude l normalized by the number of stars in the Hercules region. We can clearly see that the Hercules region contains relatively more stars in the di-

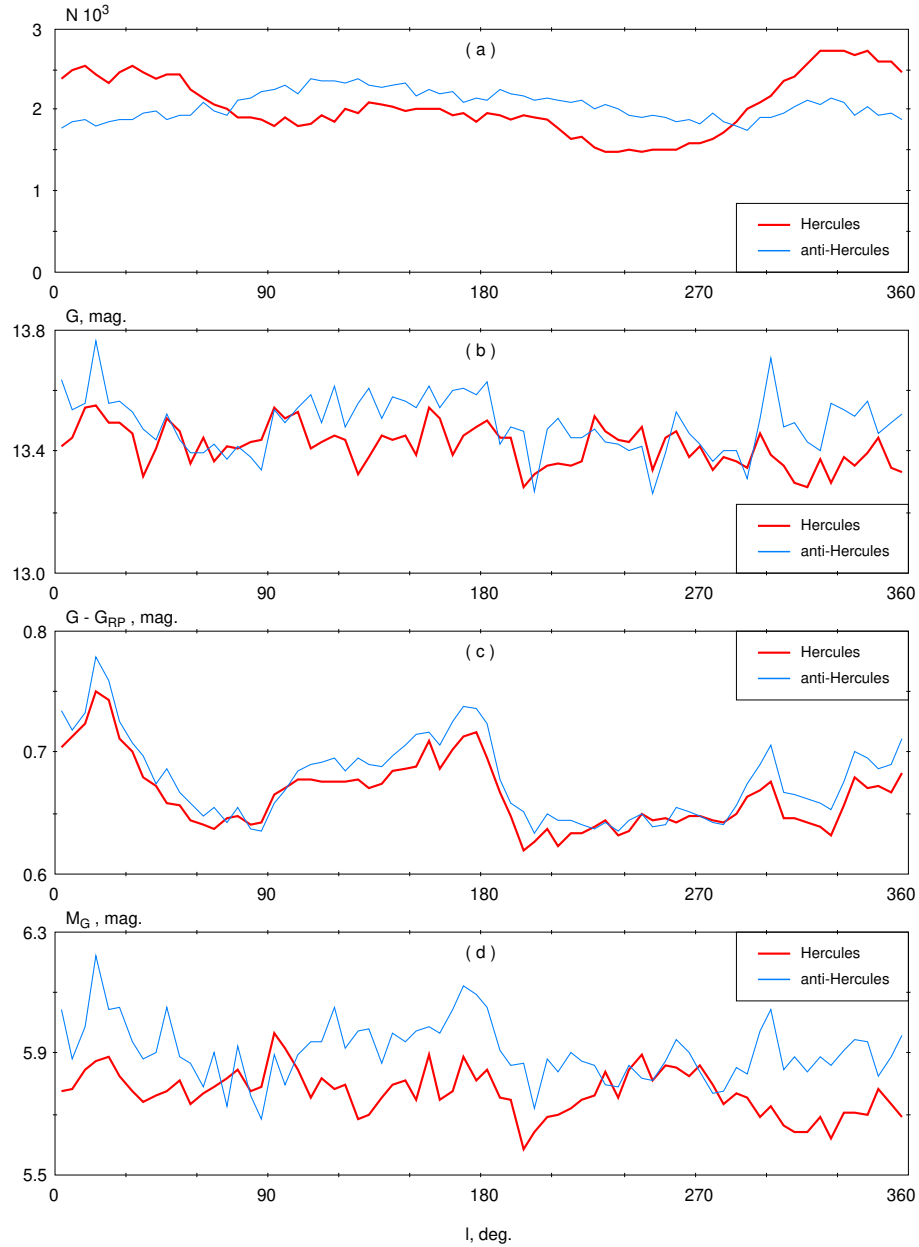


Fig. 12. Distributions of the (a) number of stars, N , (b) magnitude, G , (c) color, $G - G_{RP}$, and (d) absolute magnitude, M_G , of stars in the Hercules (red line) and anti-Hercules (blue line) regions along the Galactic longitude l , calculated from Gaia DR3 data. The values of N and the median values of G , $G - G_{RP}$, and M_G were calculated in sectors of the $\Delta l = 5^\circ$ width. (a) It is clearly seen that the Hercules region contains relatively more stars in the direction toward the Galactic center, $l < 60 \cup l > 300^\circ$, than the anti-Hercules region. (b) In the direction toward the Galactic center, $l < 45 \cup l > 300^\circ$, and in the second quadrant, $90 < l < 180^\circ$, stars of the Hercules region are, on average, brighter than those of the anti-Hercules region while in other directions the brightness of stars in both regions is approximately the same. (c) Almost everywhere, stars of the Hercules region are, on average, bluer in color than those of the anti-Hercules region. (d) The Hercules region includes more luminous stars than the anti-Hercules one almost everywhere.

rection toward the Galactic center, $l < 60 \cup l > 300^\circ$, than the anti-Hercules region while anti-Hercules region has an excess of stars in other directions, $60 < l < 300^\circ$. The excess of stars of the Hercules region in the direction toward the Galactic center may be related to the orbits shown in Fig. 7a which cross the solar neighborhood, $r < 0.5$ kpc, at the edge closest to the Galactic center. We carried out experiments by excluding stars lying in different sectors of the longitude l , including the central sector, $l < 60 \cup l > 300^\circ$, but this did not result in the disappearance of the excess of stars of the Hercules region at the top of the main sequence (Fig. 10a).

Fig. 12b shows the distributions of the median magnitude G of stars in the Hercules and anti-Hercules regions calculated in sectors along the longitude l . It is clearly seen that in the direction toward the Galactic center, $l < 45 \cup l > 315^\circ$, and in the second quadrant, $90 < l < 180^\circ$, stars in the Hercules region are, on average, brighter than in the anti-Hercules region while in other directions, the brightness of the stars in both samples is approximately the same.

Fig. 12c shows the distributions of the color of stars, $G - G_{RP}$, in the Hercules and anti-Hercules regions. Interestingly, stars in both regions are redder in the direction toward the Galactic center, $l < 45 \cup l > 315^\circ$, and in the second quadrant, $90 < l < 180^\circ$, while in the third quadrant, $180 < l < 270^\circ$, there is a sharp blueing of stars of both samples. Note, that almost everywhere, stars in the Hercules region are, on average, bluer than in the anti-Hercules region.

Fig. 12d shows the distributions of the absolute magnitude, M_G . It is clearly seen that almost everywhere the Hercules region includes more luminous stars than the anti-Hercules region. The exceptions are two sectors: $70 < l < 110^\circ$ and $230 < l < 290^\circ$, where the median M_G values are nearly the same in both regions. Note also that stars in the Hercules region are located, on average, farther away from the Sun than in the anti-Hercules region, the median estimates of the heliocentric distances r in these regions are $r = 338.7 \pm 0.3$ and 321.5 ± 0.4 pc, respectively.

The differences in the brightness, color, and luminosity of stars in the Hercules and anti-Hercules regions are possibly caused by different concentrations of these stars in the sky relative to the Galactic plane, which leads to an underestimation of the number of faint stars in the Hercules region compared to the anti-Hercules region. In general, the lack of stars with measured line-of-sight velocities in the Hercules region compared to the anti-Hercules one must result in an underestimation of the f_g value derived from the Gaia DR3 data (Eq. 1).

5. CONCLUSIONS

We studied the formation of the Hercules stream using the model of the Galaxy with an analytical bar. The model disk forms an outer resonance ring R_1R_2 located near the OLR of the bar. This model reproduces well the distributions of the radial, V_R , and azimuthal, V_T , stellar velocities along the Galactocentric distance, R , derived from the Gaia EDR3 and Gaia DR3 data. The positions of the Sun and the OLR radius of the bar correspond to the distances of $R_0 = 7.5$ and $R_{OLR} = 7.0$ kpc (Melnik et al., 2021; Melnik, Podzolkova, and Dambis, 2023).

We analyzed variations in the number of model stars in the Hercules and anti-Hercules regions over time (Fig. 2). We need the anti-Hercules region for the calibration of the number of stars. A strict definition of the Hercules and anti-Hercules regions includes two criteria. First, during the time period considered, stars must fall into the solar neighborhood, $r < 0.5$ kpc. Second, these stars must have velocities, V_R and V_T , that lie on the (V_R, V_T) plane inside ellipses centered at $V_R = 25$ and $V_T = 200$ km s $^{-1}$ (Hercules), or at $V_R = -25$ and $V_T = 200$ (anti-Hercules), with semi-axes of $\Delta V_R = 15$ and $\Delta V_T = 12$ km s $^{-1}$. The velocities V_R and V_T are calculated relative to the Galactic center.

The number of stars in the Hercules region, N_H , reaches its first maximum at the time period of 2.0–2.6 Gyr from the start of simulation and then decreases. The second maximum N_H corresponds to the period of 4.3–5.2 Gyr and looks more like a plateau. It is interesting that the number of stars N_H reaches its maximum precisely at those time periods when the humps on the V_R -velocity distributions along R disappear (2.5 ± 0.3 and 4.5 ± 0.5 Gyr), and the model best agrees with observations (Melnik and Podzolkova, 2024).

The number of stars in the anti-Hercules region, N_{aH} , demonstrates well-defined oscillations with the period of $P = 1.8 \pm 0.1$ Gyr. These oscillations are probably related to orbital librations near the OLR with the period close to $P \approx 2.0$ Gyr (Melnik, Podzolkova, and Dambis, 2023; Melnik and Podzolkova, 2024).

We calculated the relative difference, f , in the number of stars in the Hercules and anti-Hercules regions (Eq. 1), which does not depend on the number of stars in the model and observational samples. The value of f calculated for model-disk stars oscillates in the range $[-0.009, 0.656]$, and its average value is $\bar{f} = 0.291 \pm 0.011$, which is quite close to the value of $f_g = 0.315 \pm 0.004$ obtained for stars from the Gaia DR3 catalog (Fig. 3). Thus, there are many times when the model values of f coincide with the observational value f_g . On the other hand, contamination of the observational sample with thick-disk and halo stars may lead to an underestimation of the f_g value.

We investigated the orientation of orbits of model-disk stars in the Hercules and anti-Hercules regions at the time period $t = 2.5\text{--}2.6$ Gyr from the start of simulation. We divided model stars into three groups depending on the orientation of their orbits: elliptical orbits, i. e. orbits with the order of symmetry $n_s = 2$, elongated perpendicular to the bar ($75 \leq \theta_{00} < 105^\circ$); elliptical orbits ($n_s = 2$) elongated parallel to the bar ($0 \leq \theta_{00} < 15^\circ$ or $165 \leq \theta_{00} < 180^\circ$); and other orbits. The angle θ_{00} determines the average orientation of the orbit relative to the major axis of the bar during the time period $t = 0\text{--}3$ Gyr. It turned out that in the Hercules region 84% of orbits have an elliptical shape and are elongated perpendicular to the bar while in the anti-Hercules region 68% of orbits have $n_s = 2$ and are elongated parallel to the bar (Fig. 4, 5). This strongly differs from the distribution of all stars that fall in the solar vicinity, $r < 0.5$ kpc, during the period considered: 21% have elliptical orbits elongated perpendicular to the bar, and 19% have elliptical orbits elongated parallel to the bar.

We studied the distribution of stars in the Hercules and anti-Hercules regions along the initial distances $R(0)$, as well as variations in the initial radial, $V_R(0)$, and azimuthal, $V_T(0)$, velocities with variations in $R(0)$ (Fig. 6). The median values of the initial distances $R(0)$ in the Hercules and anti-Hercules regions are 6.8 and 7.3 kpc, respectively, i.e. most stars arrive in the Hercules region from the distances smaller than the OLR radius ($R_{OLR} = 7.0$ kpc) and in the anti-Hercules region from distances larger than R_{OLR} . The median values of the initial azimuthal velocity V_T calculated in bins along $R(0)$ decrease with increasing $R(0)$, although there is a small plateau (7.0–8.0 kpc) in the Hercules region. As for the initial radial velocity, the bins with maximum number of particles N correspond to the velocity $V_R(0) \approx 0$, which is in good agreement with the fact that the most probable value of the initial radial velocity in the model disk is zero.

In our previous papers, we showed that the period P of slow variations in the angular momentum, L , and total energy, E , of a star coincides with the period of variations in the direction of orbit elongation, mean size and eccentricity of the orbit (Melnik, Podzolkova, and Dambis, 2023; Melnik and Podzolkova, 2024).

In the Hercules region, there are two types of orbits (Fig. 7a and Fig. 7b). Orbits of the first type (Fig. 7a) change orientation, size, and eccentricity with a period of $P \approx 0.7$ Gyr but always lie inside a figure bounded by two ellipses elongated perpendicular to the bar. The direction of elongation of these orbits shifts only in the direction of the Galactic rotation (Fig. 8A). Orbits of the second type (Fig. 7b) are elongated at the angles $\theta_0 \approx -60^\circ$ or 60° to the major axis of the bar most of

the time, and parallel to the bar for a small part of the time. These orbits librate relative to the major axis of the bar in the range of angles $[-60, 60^\circ]$ with a period of $P \approx 2.6$ Gyr (Fig. 8B). Perhaps these orbits cause an increase in the number of stars, N_H , in the Hercules region at the time period of 2–3 Gyr (Fig. 3a).

The orbits in the anti-Hercules region librate relative to the major axis of the bar in the range of angles $[-45, 45^\circ]$ with the period of $P \approx 1.9$ Gyr (Fig. 7c and Fig. 7d). Note that librations of the orbits shown in Fig. 7c cause periodic changes in the morphology of the outer rings and the appearance of humps on the profiles of the V_R -velocity distribution along the distance R (Melnik, Podzolkova, and Dambis, 2023; Melnik and Podzolkova, 2024).

On average, orbits in the Hercules region are elongated perpendicular to the bar and support the outer ring R_1 while orbits in the anti-Hercules region are elongated parallel to the bar and support the outer ring R_2 .

We investigated the distribution of the number of orbits along the period P of slow oscillations in the angular momentum in the Hercules and anti-Hercules regions (Fig. 9). In the Hercules region, the distribution appears to have two maxima, corresponding to $P = 0.7$ and 2.6 Gyr. Probably, such a two-humped distribution is connected with two types of orbits in the Hercules region (Fig. 7a and Fig. 7b). In the anti-Hercules region, the distribution has a well-defined maximum at the period of $P = 1.9$ Gyr, which coincides with the most probable value of the period P of librating orbits near the OLR (Melnik and Podzolkova, 2024).

Analysis of the Gaia DR3 data showed that the Hercules region includes an excess of stars in the upper part of the main sequence of the Hertzsprung-Russell diagram compared to the anti-Hercules region (Fig. 10a, Table 1). This result may be caused by a lack of faint stars in the Hercules region, which leads to an increasing fraction of bright stars in this sample. The difference in the relative abundance of bright stars in the Hercules and anti-Hercules regions may be due to the fact that stars in the Hercules region are more concentrated in the sky toward the Galactic plane, which makes it difficult for the Gaia spectrometer to measure their line-of-sight velocities (Fig. 11). In general, the selection effects must also reduce the value of f_g derived from the Gaia DR3 data (Section 4.7).

ACKNOWLEDGEMENTS

We thank A. K. Dambis for fruitful discussion and helpful suggestions. We thank the anonymous reviewer for helpful comments and interesting discussion. The study was conducted under the state assignment of Lomonosov Moscow State University. This work was carried out using data from the European Space Agency (ESA) mission *Gaia* (<https://www.cosmos.esa.int/gaia>), processed by the Data Processing and Analysis Consortium (DPAC, <https://www.cosmos.esa.int/web/gaia/dpac/consortium>) *Gaia*.

DPAC support was provided by national institutions, in particular institutions participating in the multilateral agreement *Gaia*. E. N. Podzolkova is the recipient of a scholarship from the Foundation for the Development of Theoretical Physics and Mathematics "BASIS" (Grant No. 21-2-2-44-1).

REFERENCES

- R. Andrae, et al., *Astron. Astrophys.* **616**, 8 (2018)
- T. Antoja, A. Helmi, W. Dehnen, et al., *Astron. Astrophys.* **563**, 60 (2014)
- E. Athanassoula, O. Bienayme, L. Martinet, D. Pfenniger, *Astron. Astrophys.* **127**, 349 (1983)
- C. Babusiaux et al. (Gaia Collab.), *Astron. Astrophys.* **616**, 10 (2018)
- T. Bensby, M. S. Oey, S. Feltzing, and B. Gustafsson, *Astrophys. J.* **655**, L89 (2007)
- E. Bica, C. Bonatto, B. Barbuy, and S. Ortolani, *Astron. Astrophys.* **450**, 105 (2006)
- J. Binney and S. Tremaine, *Galactic Dynamics*, 2nd ed. (Princeton Univ. Press, Princeton, NJ, 2008)
- J. Bland-Hawthorn and O. Gerhard, *Astron. Astrophys. Rev.* **54**, 529 (2016)
- D. L. Block, I. Puerari, J. H. Knapen, et al., *Astron. Astrophys.* **375**, 761 (2001)
- A. Boehle, A. M. Ghez, R. Schödel, et al., *Astrophys. J.* **830**, 17 (2016)
- D. Boubert and A. Everall, *Mon. Not. R. Astron. Soc.* **497**, 4246 (2020)
- R. L. Branham, *Astrophys. Space Sci.* **362**, 29 (2017)
- A. G. A. Brown et al. (Gaia Collab.), *Astron. Astrophys.* **649**, A1 (2021)
- R. Buta, *Astrophys. J. Suppl. Ser.* **96**, 39 (1995)
- R. Buta and F. Combes, *Fund. Cosmic Physics* **17**, 95 (1996)
- R. Buta and D. A. Crocker, *Astron. J.* **102**, 1715 (1991)
- R. Buta, E. Laurikainen, and H. Salo, *Astron. J.* **127**, 279 (2004)
- G. Byrd, P. Rautiainen, H. Salo, R. Buta, D. A. Crocker, *Astron. J.* **108**, 476 (1994)
- A. Castro-Ginard, A. G. A. Brown, Z. Kostrzewa-Rutkowska, et al., *Astron. Astrophys.* **677**, 37 (2023)
- D. Chakrabarty and I. V. Sideris, *Astron. Astrophys.* **488**, 161 (2008)
- C. Chiappini, F. Matteucci, and D. Romano, *Astrophys. J.* **554**, 1044 (2001)
- R. Chiba, J. Friske, and R. Schönrich, *Mon. Not. R. Astron. Soc.* **500**, 4710 (2021)
- G. Contopoulos and P. Grosbøl, *Astron. Astrophys. Rev.* **1**, 261 (1989)
- G. Contopoulos and Th. Papayannopoulos, *Astron. Astrophys.* **92**, 33 (1980)
- A. K. Dambis, L. N. Berdnikov, A. Y. Kniazev, et al. *Mon. Not. R. Astron. Soc.* **435**, 3206 (2013)
- W. Dehnen, *Astron. J.* **115**, 2384 (1998)
- W. Dehnen, *Astron. J.* **119**, 800 (2000)
- G. de Vaucouleurs and K. C. Freeman, *Vis. in Astron.* **14**, 163 (1972)
- S. Díaz-García, H. Salo, E. Laurikainen, and M. Herrera-Endoqui, *Astron. Astrophys.* **587**, 160 (2016)
- R. Drimmel, S. Khanna, E. D'Onghia, et al. *Astron. Astrophys.* **670**, 10 (2023)
- O. J. Eggen, *Mon. Not. R. Astron. Soc.* **118**, 154 (1958)
- F. Eisenhauer, R. Genzel, T. Alexander, et al., *Astrophys. J.* **628**, 246 (2005)
- A. Everall and D. Boubert, *Mon. Not. R. Astron. Soc.* **50**, 6205 (2022)
- M. W. Feast, C. D. Laney, T. D. Kinman, F. van Leeuwen, and P. A. Whitelock, *Mon. Not. R. Astron. Soc.* **386**, 2115 (2008)
- F. Fragkoudi, D. Katz, W. Trick, et al. *Mon. Not. R. Astron. Soc.* **488**, 3324 (2019)
- Ch. Francis and E. Anderson, *Mon. Not. R. Astron. Soc.* **441**, 1105 (2014)
- R. Fux, *Astron. Astrophys.* **373**, 511 (2001)
- E. V. Glushkova, A. K. Dambis, A. M. Melnik, and A. S. Rastorguev, *Astron. Astrophys.* **329**, 514 (1998)
- M. A. T. Groenewegen, A. Udalski, and G. Bono, *Astron. Astrophys.* **481**, 441 (2008)
- K. Hattori, N. Gouda, H. Tagawa, N. Sakai, T. Yano, J. Baba, and J. Kumamoto, *Mon. Not. R. Astron. Soc.* **484**, 4540 (2019)
- J. A. S. Hunt, et al., *Mon. Not. R. Astron. Soc.* **474**, 95 (2018)
- P. Iwanek, R. Poleski, S. Kozłowski, et al., *Astrophys. J. Suppl. Ser.* **264**, 20 (2023)
- D. Katz et al. (Gaia Collab.), *Astron. Astrophys.* **616**, A11 (2018)
- X. Liang, S.-J. Yoon, J. Zhao, Z. Li, J. Zhang, and Y. Wu, *Astrophys. J.* **956**, 146 (2023)
- S. Lucchini, E. Pellett, E. D'Onghia, and J. A. L. Aguerri, *Mon. Not. R. Astron. Soc.* **519**, 432 (2023)
- A. M. Melnik, *Mon. Not. R. Astron. Soc.* **485**, 2106 (2019)
- A. M. Melnik and A. K. Dambis, *Astrophys. Space Sci.* **365**, 112 (2020)
- A. M. Melnik, A. K. Dambis, E. N. Podzolkova, L. N. Berdnikov, *Mon. Not. R. Astron. Soc.* **507**, 4409 (2021)
- A. M. Melnik and E. N. Podzolkova, *Astron. Lett.* **50**, 481 (2024)
- A. M. Melnik, E. N. Podzolkova, and A. K. Dambis, *Mon. Not. R. Astron. Soc.* **525**, 3287 (2023)
- A. M. Melnik and P. Rautiainen, *Astron. Lett.* **35**, 609 (2009)

- T. A. Michtchenko, J. R. D. Lepine, A. Perez-Villegas, R. S. S. Vieira, and D. A. Barros, *Astrophys. J.* **863**, L37 (2018)
- I. Minchev, J. Nordhaus, and A. C. Quillen, 2007, *Astrophys. J.* **664**, L31
- G. Monari, B. Famaey, A. Siebert, A. Duchateau, T. Lorscheider, and O. Bienayme, *Mon. Not. R. Astron. Soc.* **465**, 1443 (2017)
- I. I. Nikiforov, *ASP Conf. Ser.* **316**, 199 (2004)
- S. Nishiyama, T. Nagata, S. Sato, et al., *Astrophys. J.* **647**, 1093 (2006)
- A. Perez-Villegas, M. Portail, Ch. Wegg, and O. Gerhard, *Astrophys. J.* **840**, L2 (2017)
- D. Pfenniger, *Astron. Astrophys.* **134**, 373 (1984)
- T. Prusti, et al. (Gaia Collab.), *Astron. Astrophys.* **595**, A1 (2016)
- A. C. Quillen, G. De Silva, S. Sharma, et al., *Mon. Not. R. Astron. Soc.* **478**, 228 (2018)
- P. Ramos, T. Antoja, and F. Figueras, *Astron. Astrophys.* **619**, 72 (2018)
- P. Rautiainen and A. M. Melnik, *Astron. Astrophys.* **519**, 70 (2010)
- P. Rautiainen and H. Salo, *Astron. Astrophys.* **348**, 737 (1999)
- P. Rautiainen and H. Salo, *Astron. Astrophys.* **362**, 465 (2000)
- M. J. Reid, K. M. Menten, X. W. Zheng, A. Brunthaler, and Y. Xu, *Astrophys. J.* **705**, 1548 (2009)
- J. Rybizki, H.-W. Rix, M. Demleitner, C. Bailer-Jones, and W. J. Cooper, *Mon. Not. R. Astron. Soc.* **500**, 397 (2021)
- M. P. Schwarz, *Astrophys. J.* **247**, 77 (1981)
- W. H. Trick, F. Fragkoudi, J. A. S. Hunt, J. T. Mackereth, and S. D. M. White, *Mon. Not. R. Astron. Soc.* **500**, 2645 (2021)
- A. Vallenari et al. (Gaia Collab.), *Astron. Astrophys.* **674**, A1 (2023)
- M. D. Weinberg, *Astrophys. J.* **420**, 597 (1994)